Article

Direct Growth of Nitrogen-Doped Carbon Quantum Dots on Co_9S_8 Passivated on Cotton Fabric as an Efficient Photoelectrode for Water Treatment

Kinza Shahid, Mubark Alshareef, Mumtaz Ali, Muhammad Imran Yousaf,* Marwah M. Alsowayigh, and Imtiaz Afzal Khan

Read Online

ACCESS | Metrics & More | Article Recommendations | SI Supporting Information

ABSTRACT: Heterogeneous growth of photocatalysts on different porous substrates is a solution to avoid secondary pollution caused by composite photocatalysts themselves. However, the heterogeneous growth of composite photocatalysts with nitrogen-doped carbon quantum dots (NCQDs) inclusions—introduced during synthesis—impedes the direct growth on the substrate. To overcome this problem, NCQDs were grown on a Co_9S_8 (NCQDs-G@Co_9S_8) layer, decorated on cotton fabric. This optimal coupling mode of NCQDs and Co_9S_8 showed 54% degradation, compared to 33% dye degradation via NCQDs-doped Co_9S_8 (NCQDs-D@Co_9S_8). The change in the crystal structure and its lower loading on fabric results in significantly lower performance of NCQDs-D@Co_9S_8. Even with the combination of both surface growth and doping (NCQDs-DG@Co_9S_8), the performance was still limited to 42%. In addition, the optimum growth concentration of NCQDs on Co_9S_8 was observed for 7.5 w/w %, resulting in 92% photocatalytic activity (PCA) in 80 min. Comparing different surface states formed in NCQDs using different solvents, water-based surface states (oxygen-rich surface) are most suitable for the dye degradation. NCQDs-G@Co_9S_8 also offers 67% Cr-VI reduction to Cr-III, showing its suitability for both inorganic and organic compounds. Better electrode performance was related to suitable charge separation of the composite, where —OH groups mainly contribute in the photocatalytic dye degradation..
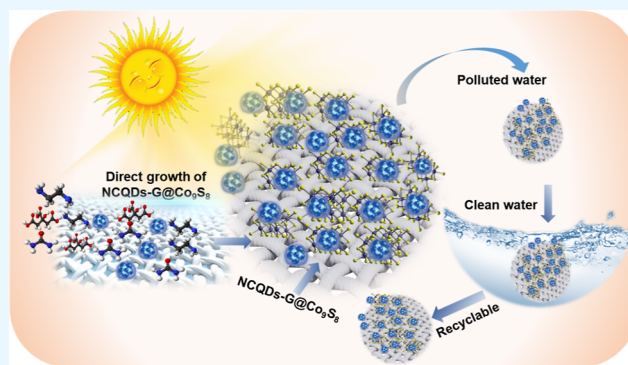
1. INTRODUCTION

Organic dyes, which are commonly used in several productions such as textile dyeing, paints, inks, plastics, food, pharmaceuticals, and cosmetics, are being discharged into water bodies even after treatment, leading to water pollution.[1] In particular, textile industry is a major contributor to this environmental issue due to the release of nonbiodegradable dye effluents. The anaerobic breakdown of certain N-group-containing dyes, such as Rhodamine B (RhB) and methylene blue (MB), can produce carcinogenic substances and it is important to find ways to reduce these dyes into noncontaminated components in order to address this environmental concern.[2] Several techniques are commonly used to treat wastewater, including precipitation, chemical oxidation, coagulation—flocculation, adsorption, purification, and reverse osmosis.[3] Recently, photocatalyst materials using daylight energy for the degradation of organic dyes has emerged as a potential solution. In the process, semiconductors, such as metal sulfides and oxides, absorb sunlight and an electron—hole pair is generated, enabling the destruction of organic compounds and reduction of inorganic moieties.[4]

Initially, researchers were focused on the use of various semiconductor metal sulfide nanostructures, including ZnS, CdS, CuS, Ag_2S, Bi_2S_3, CoS, FeS, and PbS, as photocatalysts in the degradation of dyes under UV—visible solar irradiation.[5] These materials have fast charge recombination; hence, the heterojunctions of these materials with carbon quantum dots (CQDs) are developed.[6] Compared to traditional metals-based quantum dots, CQDs offer low cost, biocompatibility, and zero-photobleaching. CQDs are a mixture of sp^2 and sp^3 hybridized carbon, with excessive surface functional groups.[7] Due to their extreme small size, CQDs colloid is difficult to recover from treated water; therefore, CQDs are commonly coupled with other nanomaterials or nano substrates to ensure their ease of recovery and suppress their fast charge

recombination.[8] Because of $\pi-\pi^*$ (C=C) and $n-\pi^*$ (C—O, C—N) transitions, CQDs revealed a broad ultraviolet absorption with a tail in the visible region.[9] As a result, CQDs may extend the visible light range of wide band gap semiconductor photocatalyst light utilization range. Amorphous and nanocrystalline cores containing primarily graphitic or turbostratic carbon (sp^2 carbon) or graphene and graphene oxide sheets joined by diamond-like sp^3 hybridized carbon insertions make up the typical quasi-spherical nanoparticles known as CQDs.[10] The CQDs may have a unique ability with better electron transport and reservoir properties as a result. CQDs have been employed to develop photocatalysts with increased activity by combining with semiconductor nanoparticles including TiO_2, CdS, Fe_2O_3, $g-C_3N_4$, Ag_3PO_4, Cu_2O, and Bi_2WO_6 as a potent energy-transfer component.[11,12] Doping CQDs with elements such as N and P, the photocatalytic activity (PCA) of CQDs can be further improved.[13] For instance, nitrogen-doped carbon quantum dots (NCQDs) synthesized from fruit bunches and urea showed highly effective photocatalysts for degrading methyl green. Under 302 nm UV lamp irradiation, NCQDs were able to degrade 99.91% of the methyl green, a much higher rate than that achieved by CQDs (39.27%).[14] Similarly, NCQDs were doped in TiO_2 and showed 7.3 times higher photocatalysis for RhB dye due to better light absorption. Similarly, the heterogeneous growth of NCQDs on reduced graphene oxide and carbon nanotubes was studied to enhance the photoactivity of the composite structure.[15] These conductive substrates provide suitable charge mobility, thus suppressing the charge recombination of NCQDs.[16] In the heterojunction photocatalytic composites, NCQDs enhance the photoactivity via increasing the surface area, better charge separation, and enhanced surface reactivity.[17] CQDs are recognized for their photoinduced electron transfer and photoluminescence properties.[18] N-doped ZnO was decorated with CQDs to improve the photocatalytic performance of the photocatalyst.[19] The combination of N-doped ZnO and CQDs was found to be effective in promoting charge separation, preventing charge recombination, and increasing photocatalytic efficiency and antiphotocorrosion. This combination is considered an ideal approach to enhance the performance of photocatalysts.[20]

The heterogeneous growth of composite structures on different substrates is an ultimate solution to resolve the issues related to secondary pollution caused by nanocomposites their self.[21] However, doping of NCQDs during the synthesis of nanomaterials suppress the heterogeneous growth on substrate and promote the homogeneous growth in solution.[22] To overcome this problem, we synthesized a composite of Co_9S_8 with NCQDs via heterogeneous growth (NCQDs-G@Co_9S_8), i.e., after synthesis of Co_9S_8 on fabric, followed by NCQDs direct growth on Co_9S_8. This optimal coupling mode between NCQDs and Co_9S_8 resulted in 54% degradation, which was higher than the 33% degradation observed with NCQDs-doped Co_9S_8 (NCQDs-D@Co_9S_8). The lower performance of NCQDs-D@Co_9S_8 was due to changes in the crystal structure and reduced loading on the fabric. Even if NCQDs were grown on the doped CQDs composite (NCQDs-DG@Co_9S_8), the performance was limited to 42%. The optimum loading content of NCQDs-G@Co_9S_8 resulted in 92% PCA within 80 min, when the concentration of NCQDs on Co_9S_8 was 7.5 w/w %. In addition, we also studied the role of different surface states of CQDs by changing the reaction solvents. The oxygen-rich surface obtained by using water as reaction solvent showed

highest PCA.[23] Moreover, NCQDs-G@Co_9S_8 with the optimum concentration also exhibited 67% reduction of Cr-VI to Cr-III, indicating its suitability for both organic and inorganic pollutants.

2. MATERIALS AND METHODS

Required chemicals for the synthesis of cobalt sulfide (Cobalt Nitrate, Thiourea) were purchased from Sigma-Aldrich. Other chemicals required for the synthesis of NCQDs, including citric acid, ethylenediamine, and ethanol were also obtained from Sigma-Aldrich. Deionized water and thoroughly washed glassware were used throughout the experiment.

2.1. Cobalt Sulfide Synthesis. Cobalt sulfide was grown on cotton fabric using the solvothermal route, as shown schematically in Figure 1. In the preparation, 20 mL of distilled

Figure 1. Synthesis of Co_9S_8 using the hydrothermal method.

water and 80 mL of ethanol was taken in a beaker. 0.29 g of the cobalt nitrate and 0.152 g of thiourea were added into the solvent mixture. These precursors were allowed to stir for 1 h at 800 rpm, to make a clear solution. This homogeneously mixed solution was transferred to Teflon-lined autoclave of 200 mL capacity and a piece of cotton (7 × 7 cm) fabric was immersed in this solution. Autoclave was set for heating in the oven at 150 °C for 8 h and allowed to cool down naturally after completion of the reaction. The fabric sample having Co_9S_8 growth was then cleaned with distilled water and was dried in the oven at 70 °C for half an hour.

2.2. NCQDs Doping and Growth on Cobalt Sulfide Modified Fabric. NCQDs were synthesized using the hydrothermal route, as shown in Figure 2a. Three grams of citric acid, 3 g of urea, and 0.5 mL of ethylenediamine were dissolved in 100 mL water. The solution formed was placed on the magnetic stirrer for about 30 min at 800 rpm to make a clear solution. This homogeneous mixture of solution was transferred into the Teflon-lined autoclave of 200 mL capacity with a piece of grown cobalt sulfide cotton fabric added to it. The autoclave was set into the oven at 180 °C for 6 h and was allowed to cool down naturally after completion of the reaction. The sample was then filtered and purified using a dialysis membrane, followed by drying in an oven at 70 °C. NCQDs were doped in Co_9S_8 modified cotton fabric by the hydrothermal route, 20 wt % of NCQDs, 0.29 g of the cobalt nitrate, and 0.152 g of thiourea were added in to 100 mL of distilled water and stirred it for 20 min. This homogeneous mixture of solution was transferred into the Teflon-lined autoclave of 200 mL capacity with a piece of Co_9S_8 modified cotton fabric added to it at 150 °C for 8 h. The sample was then cleaned with distilled water and the fabric was dried in the oven at 70 °C.
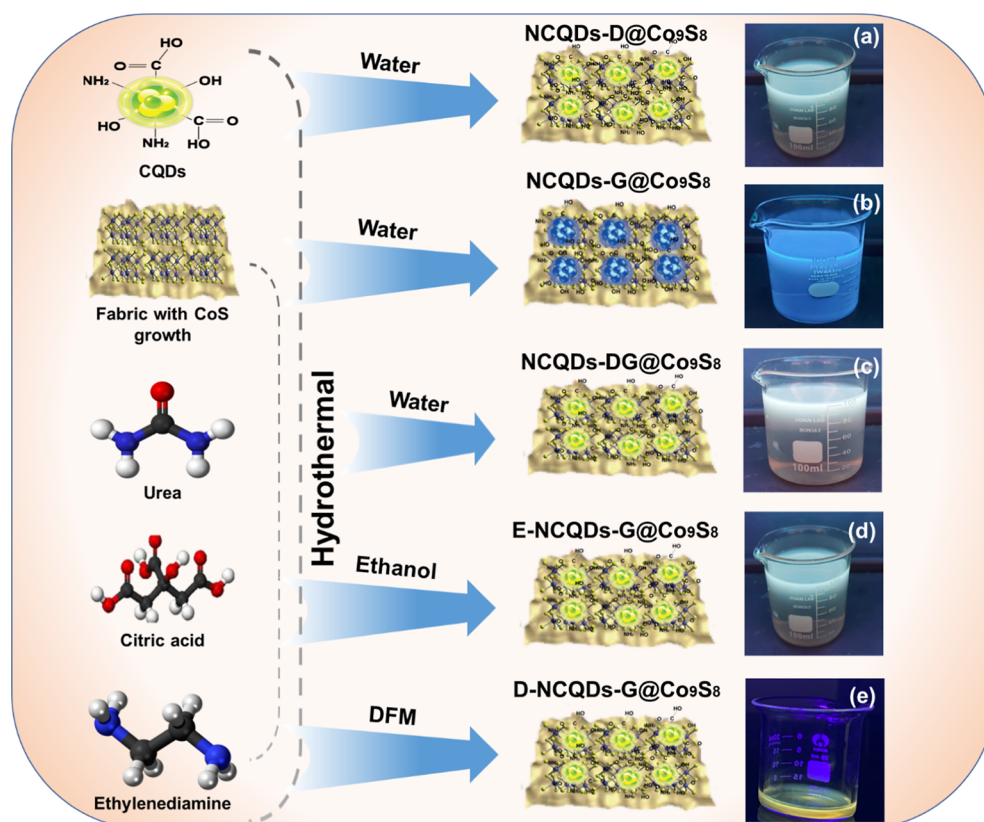
Figure 2. Synthesis method of NCQDs and Co_9S_8 composites in different solvents. (a) Doping of NCQDs in Co_9S_8 modified fabric using the hydrothermal method (NCQDs-D@Co_9S_8), (b) NCQDs growth on Co_9S_8 modified fabric (NCQDs-G@Co_9S_8), (c) NCQDs doping and growth on Co_9S_8 modified fabric (NCQDs-DG@Co_9S_8), (d) NCQDs growth on Co_9S_8 modified fabric using ethanol (E-NCQDs-DG@Co_9S_8), and (e) NCQDs growth on Co_9S_8 modified fabric using DMF (D-NCQDs-G@Co_9S_8). All NCQDs-G@Co_9S_8 were synthesized using water.

NCQDs were grown on Co_9S_8 modified cotton fabric by the hydrothermal route, as shown in Figure 2b. Elaborately, Co_9S_8 modified fabric was immersed in autoclave of NCQDs solution, which was heated in the oven at 180 °C for 8 h. During this carbonization, some NCQDs were grown on the fabric, while some of them formed in the solution. The NCQDs grown on Co_9S_8-modified fabric NCQDs-G@Co_9S_8 were rinsed to remove unattached materials and were dried for testing.

As mentioned in the above sections, a combined process of doping and growth was used to synthesize NCQDs-DG@ Co_9S_8, as shown in Figure 2c.

To check the effect of surface states, ethanol, DMF, and water were used as solvents of NCQDs synthesis to prepare E-NCQDs, D-NCQDs, and W-NCQDs, respectively. Direct growth of NCQDs on the synthesized Co_9S_8 resulted in different composite structures, respectively, using the same method (explained above). After this, the fabric was dipped in a zinc chloride (0.1 g in 100 mL deionized water) solution and dried three times at 150 °C to stop leeching off the grown material.

3. CHARACTERIZATIONS

The UV−visible absorbance spectrometer confirms the photocatalytic activity of electrode (NCQDs-G@$Co_9S_{8)}$ from Shimadzu, Japan. Transmission electron microscopy (TEM) was used to confirm the growth of NCQDs on Co_9S_8 surface, with high-resolution imaging using JEM-2100F; JEOL Ltd. Japan. Atomic spacing measurements of the NCQDs and

Co_9S_8 were calculated from grayscale TEM images. Additionally, the surface morphology of NCQDs-G@Co_9S_8 grown on cotton fabric were examined using field-emission scanning electron microscopy (FESEM) at an accelerating voltage of 15 kV, tested after Pt sputtering for 2 min. The samples were also analyzed for structural crystallinity using wide-angle X-ray diffraction (XRD) using D/MAX-2500, equipped with an X-ray source from Rigaku Corporation, Japan. Furthermore, the functional groups of NCQDs and Co_9S_8 were identified using a Fourier transform infrared (FTIR) spectrophotometer from Thermo Fisher Scientific Inc. X-ray photoelectron spectroscopy (XPS) was utilized to study the elemental composition and chemical groups in the modified carbon heterostructures with a Multilab ESCA 2000 system VG from Thermo Scientific, USA, equipped with a mono Al Ka X-ray source with an energy step size of 0.05 V. To observe optical properties of composite, the absorbance spectra of the NCQDs were recorded using a UV−visible absorbance spectrometer from Shimadzu, Japan. Using FluoTime 300, the time-resolved photoluminescence (TRPL) method was utilized to estimate the charge recombination dynamics.

4. RESULTS AND DISCUSSION

Metal chalcogenides (Co_9S_8, CuS, etc.) are gaining interest in diverse electrical, optical, and optoelectronic devices due to their extended visible spectrum absorbance and suitable band gap. However, high conductivity of Co_9S_8 causes fast charge recombination of electron/hole pairs, limiting their photocatalytic applications. Therefore, the integration of NCQDs
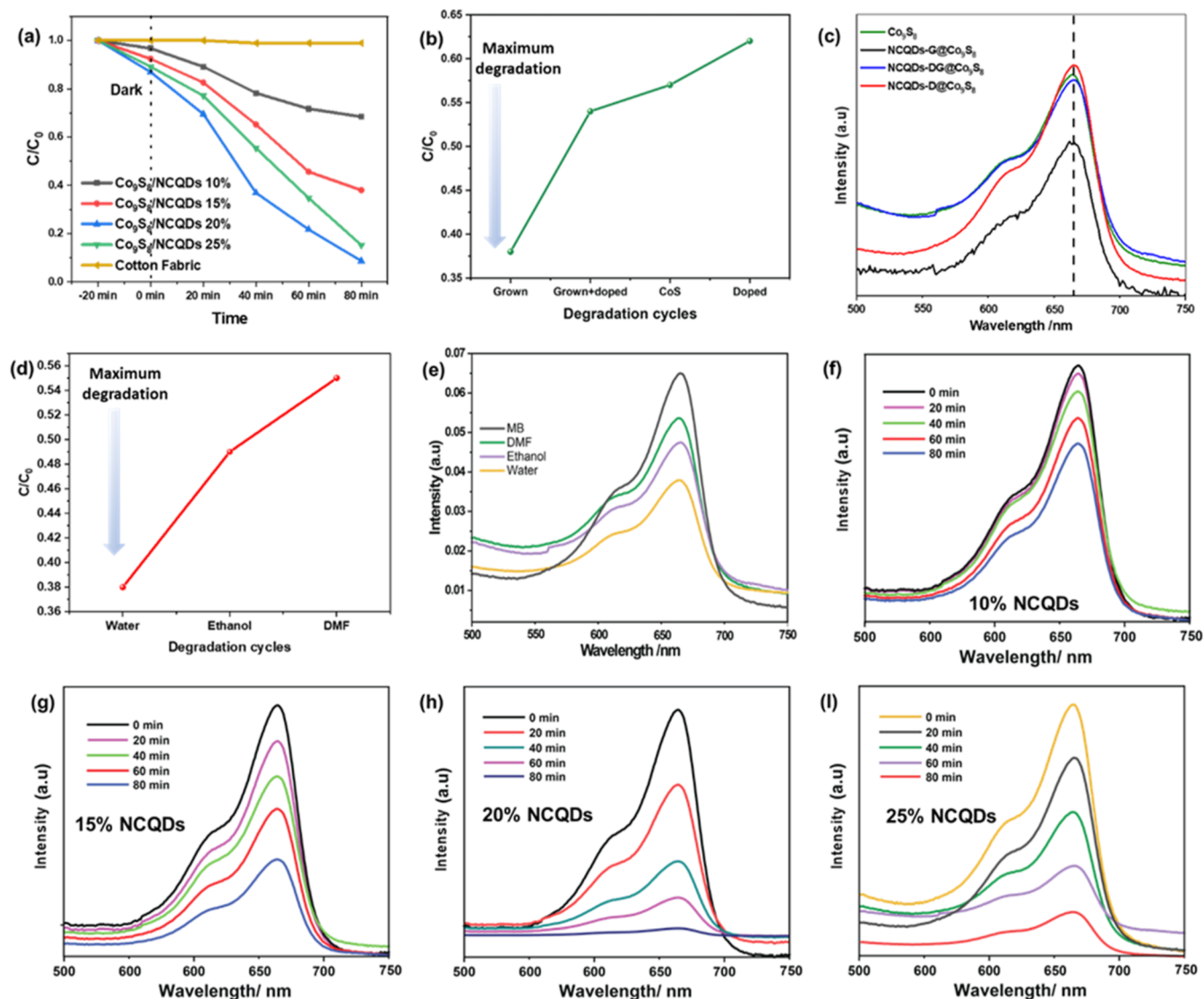
Figure 3. (a,b) Degradation concentration and degradation of Co_9S_8, NCQDs-G@Co_9S_8, NCQDs-DG@Co_9S_8, and NCQDs-D@Co_9S_8. (c,d) Degradation concentration and degradation of Co_9S_8/NCQDS synthesized using water, ethanal, and DMF. (e−i) Degradation concentration and degradation of methylene blue dye and degradation concentration.

can be considered a promising method to suppress fast recombination, achieving high-efficiency composite photocatalysts. Previously, NCQDs were doped in various semiconductors; however, such in situ doping causes the defects in the crystal structure and impedes the heterogeneous growth of Co_9S_8 on any substrate. During in situ doping, NCQDs serve as a nucleation site in the synthesis solution, thus promoting homogeneous synthesis of composite in the synthesis solution. Considering this problem, here, we proposed heterogeneous growth of NCQDs on the Co_9S_8 layer, decorated on a cotton fabric electrode.[24] The coupling modes of NCQDs with Co_9S_8 (NCQDs-D@Co_9S_8), (NCQDs-DG@Co_9S_8), and (NCQDs-G@Co_9S_8) are compared for photocatalysis, as shown in Figure 3. Higher degradation of dye is related to lower absorbance of UV−vis. We analyzed the electrode's effectiveness for methylene blue (MB) degradation.[25] This electrode was dipped in MB solution (10 mg/L). The solution samples were analyzed at 0 min and kept immersed under dark conditions to check the adsorption of the dye. Afterward, it was placed under a light source (visible 430 nm, light-emitting

diode [LED] 460 nm, and LED 525 nm). After every 20 min, the solution samples were analyzed to assess the MB degradation via UV−vis spectrophotometer. This process was repeated for 80 min.[26] The photocatalytic activity of Co_9S_8 and NCQDs-DG@Co_9S_8 compound photocatalysts in the decrease of aqueous MB under visible light (>430 nm) irradiation is given in Figure 3a. PCA of NCQDs-D@Co_9S_8, Co_9S_8, NCQDs-DG@Co_9S_8, and NCQDs-G@Co_9S_8 showed 33, 38, 42, and 54% dye degradation after 30 min, respectively. Among all coupling modes, the PCA of NCQDs-G@Co_9S_8 (heterogeneously grown NCQDs) have efficient photocatalytic activity. In addition, there was negligible dye degradation using only cotton fabric, i.e., photodegradation of MB due to light only. PCA was only observed for the samples having active materials loaded fabric substrates.

These findings indicate that the reduction in MB has a catalytic effect. Under daylight (>430 nm) irradiation for 80 min in the presence of Co_9S_8, MB degradation is slow. Instead, in the presence of Co_9S_8/NCQDs composite photocatalysts, MB reduction process is accelerated, showing 91% degrada-
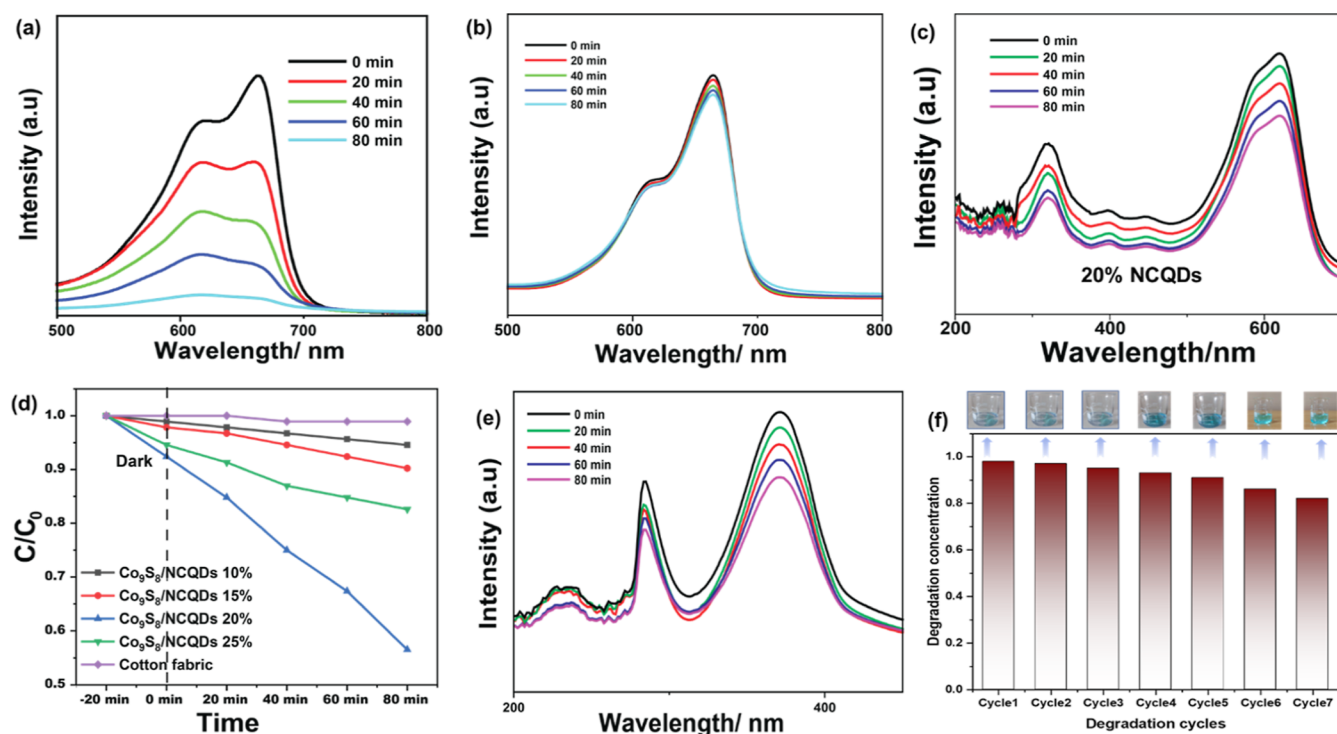
Figure 4. (a,b) Degradation of methylene blue dye in acidic and basic conditions. (c) Degradation of acid black1 using an optimized electrode (NCQDs-G@Co$_9$S$_8$). (d) Degradation concentration and degradation of (NCQDs-G@Co$_9$S$_8$). (e) Cr(IV) reduction using optimized electrode (NCQDs-G@Co$_9$S$_8$). (f) Cyclic stability of optimized composite electrode.

tion. The optimized sample NCQDs-G@Co$_9$S$_8$ showed 54 and 29% higher PCA than Co$_9$S$_8$ and NCQDs-D@Co$_9$S$_8$ (Figure 3c). This effect can be related to formation of a defect free crystal structure of Co$_9$S$_8$ without doping of NCQDs. The final MB spectra after the PCA test is shown in Figure 3d, which shows a significantly lower concentration of MB. The proposed composite structure of NCQDs provides a continuous and facile method of synthesis, as direct growth of NCQDs omits the complex purification methods of CQDs. Hence, the scalability production of composite structure is possible. In order to tune the compatibility and band alignment of NCQDs and Co$_9$S$_8$, different surface states of NCQDs were tested. These surface states were changed via variation of solvents, i.e., by using water, ethanol, and DMF.[27] These prepared samples were used to check the photocatalytic activity of electrodes as shown in Figure 4d. Considering degradation for 30 min, 54, 38, and 44% dye degradation observed using water-, DMF-, and ethanol-based NCQDs, respectively.[28] The results show that water-grown NCQDs have high photocatalytic activity and better band alignment with Co$_9$S$_8$. Although water-based NCQDs have higher band gap and lower optical absorbance;[29] however, its band structure is well aligned with the Co$_9$S$_8$. Therefore, we chose water-based NCQDs for the further optimization of nanocomposite structure in the next section.[30]

The concentration of optimized NCQDs was further varied to check the optimum PCA of the Co$_9$S$_8$/NCQDs composite. For this purpose, we changed the concentration of NCQDs precursors, which showed a significant influence in determining PCA.[31] For example, different weight percentages of NCQDs precursors (10, 15, 20, and 25 wt %) with respect to Co$_9$S$_8$ precursors were studied for PCA. It was observed that NCQDs-G@Co$_9$S$_8$ composite photocatalysts have photocatalytic activity in the order of 10% NCQDs-G@Co$_9$S$_8$ <

15% NCQDs-G@Co$_9$S$_8$ < 25% NCQDs-G@Co$_9$S$_8$ < 20% NCQDs-G@Co$_9$S$_8$. The PCA of MB using 10% NCQDs-G@Co$_9$S$_8$, 15% NCQDs-G@Co$_9$S$_8$, 20% NCQDs-G@Co$_9$S$_8$, and 25% NCQDs-G@Co$_9$S$_8$ were 34.3, 65.6, 91.4, and 85.7%, respectively, within 80 min. These photocatalytic results reveal that the photocatalytic performance of NCQDs-G@Co$_9$S$_8$ composites improved as the amount of NCQDs increased up to 20 wt % of Co$_9$S$_8$ precursors. Above this concentration, the excessive growth of NCQDs occurs, resulting in formation of aggregates and microsized NCQDs particles.[32] Therefore, based on 91% PCA of MB via 20 wt % NCQDs-G@Co$_9$S$_8$ composite, we consider it as optimum sample for photo-catalytic degradation.[33]

Processing parameters of the electrode were also taken into account for achieving better performance. Considering this, the PCA of the optimized composite electrode was tested under both acidic pH 3 and basic pH 10, as revealed in Figure 4a,b. PCA of the electrode was slightly enhanced up to 96% under basic condition, whereas acidic conditions significantly suppressed the PCA, i.e., only 33%. Hydroxyl ions are key radicals for dye degradation which increase the photolysis in the basic medium.[34] MB can absorb light in the 505−710 nm range, can create singlet and triplet species via electronic transitions and intersystem crossing, and can partially decompose itself. The degradation of MB dye occurs via photolysis, which is obtained at atmospheric pressure, meaning that O$_2$ is necessary. Monoelectronic reduction of MB$^+$ radicals by OH produces •OH radicals in basic media. H$_2$O$_2$, a crucial active species in degradation processes, is created when •OH reacts with one another.[35] Similar to how MB* radicals are stimulated, O$_2$ interacts with them to generate O$_2$•$^−$.[36] These photolysis reactions of MB are summarized in the following eqs 1−3, as follow
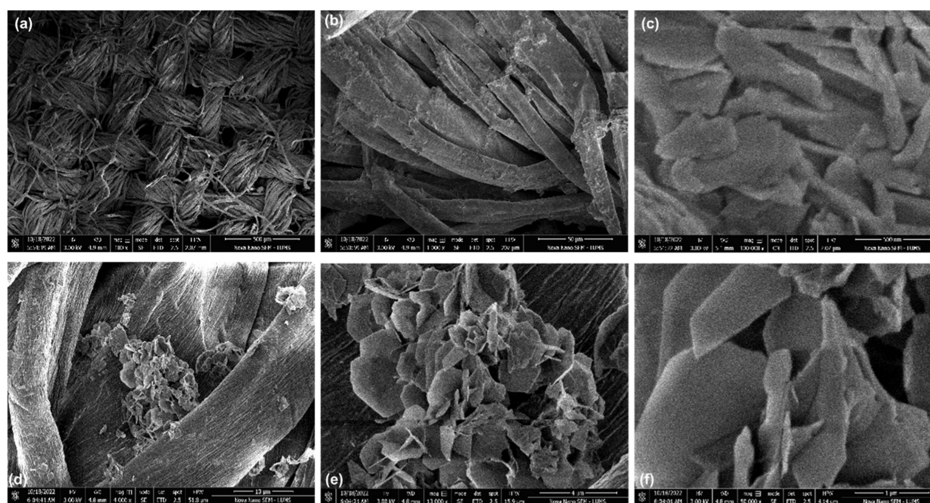
Figure 5. (a–f) SEM image of Co_9S_8 and NCQDs growth on cotton fabric.
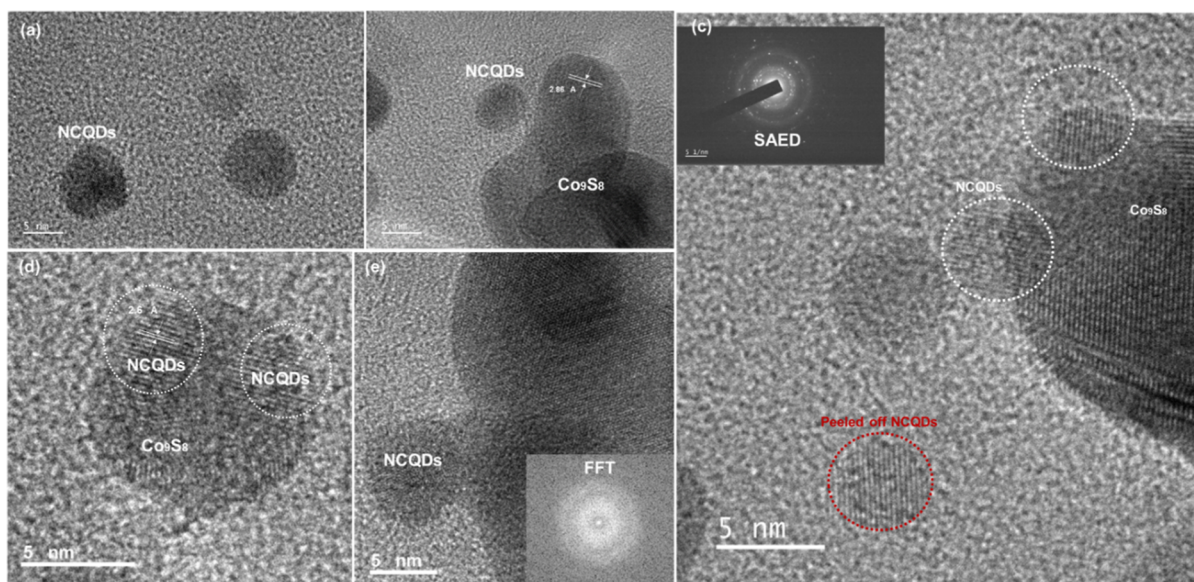
Figure 6. (a) TEM image of NCQDs. (b,d) TEM image of NCQDs-G@Co_9S_8. (c) HTEM image and SAED of NCQDs-G@Co_9S_8. (e) TEM and FFT images of Co_9S_8 and NCQDs.

$$MB^+ + OH^- \rightarrow MB^* + OH^\bullet \tag{1}$$

$$2OH^\bullet \rightarrow H_2O_2 \tag{2}$$

$$MB^* + O_2 \rightarrow MB^+ + O_2^{\bullet-} \tag{3}$$

Similar to the sensitivity of PCA of MB dye against acidic conditions, the degradation of acidic dye was also relatively low using the composite structure. For example, acid black 1 dye solution (1.90×10^{-5} mol L^{-1}) was tested for the PCA. As a result, decolorized solution proposed the rapid elimination of the dye chromophore structure ($-N{=}N-$) which showed the reduction in the absorption band at 615 nm.[37] In contrast, the absorbance at 320 nm, a wavelength commonly ascribed to aromatic structures, presented a less intense diminution. These results showed that 13, 17, 48, and 24% dye degradation using NCQDs-G@Co_9S_8 with 10, 15, 20%, and 25 wt %, as revealed in Figure 4c,d. Degradation of acid black1 is less than MB because of its acidic nature, which has lower compatibility with holes.[38] The results show that there is a maximum positive

charge present on the surface and the degradation occurs due to OH groups and holes present on the surface. So, the composite degrades MB rather than acid black1.[39]

However, because of its high mobility, high stability, difficulty in reduction, and effective toxicity, chromium, a typical heavy metal, is one of the most dangerous contaminants from leather tanning, textile dyeing, electroplating, paint, and pigment industries. 42% Cr(IV) reduction using (NCQDs-G@Co_9S_8 20%) optimized sample as shown in Figure 4e. One of the purposes of growth on a fabric substrate is the cyclic stability and reusability of the composite electrode. The reusability results revealed that the electrode retained 98, 97, 95, 93, 91, 86, and 82% of initial PCA after seven consecutive cycles as indicated in Figure 4f. This shows the stability of the electrode for practical applications, where easier separation is possible, without using filtration or centrifugation, as commonly employed for mobile phase photocatalysts.[40] The advantage of direct growth also lies in high performance and stability, as compared to use of binders. The binders passivate
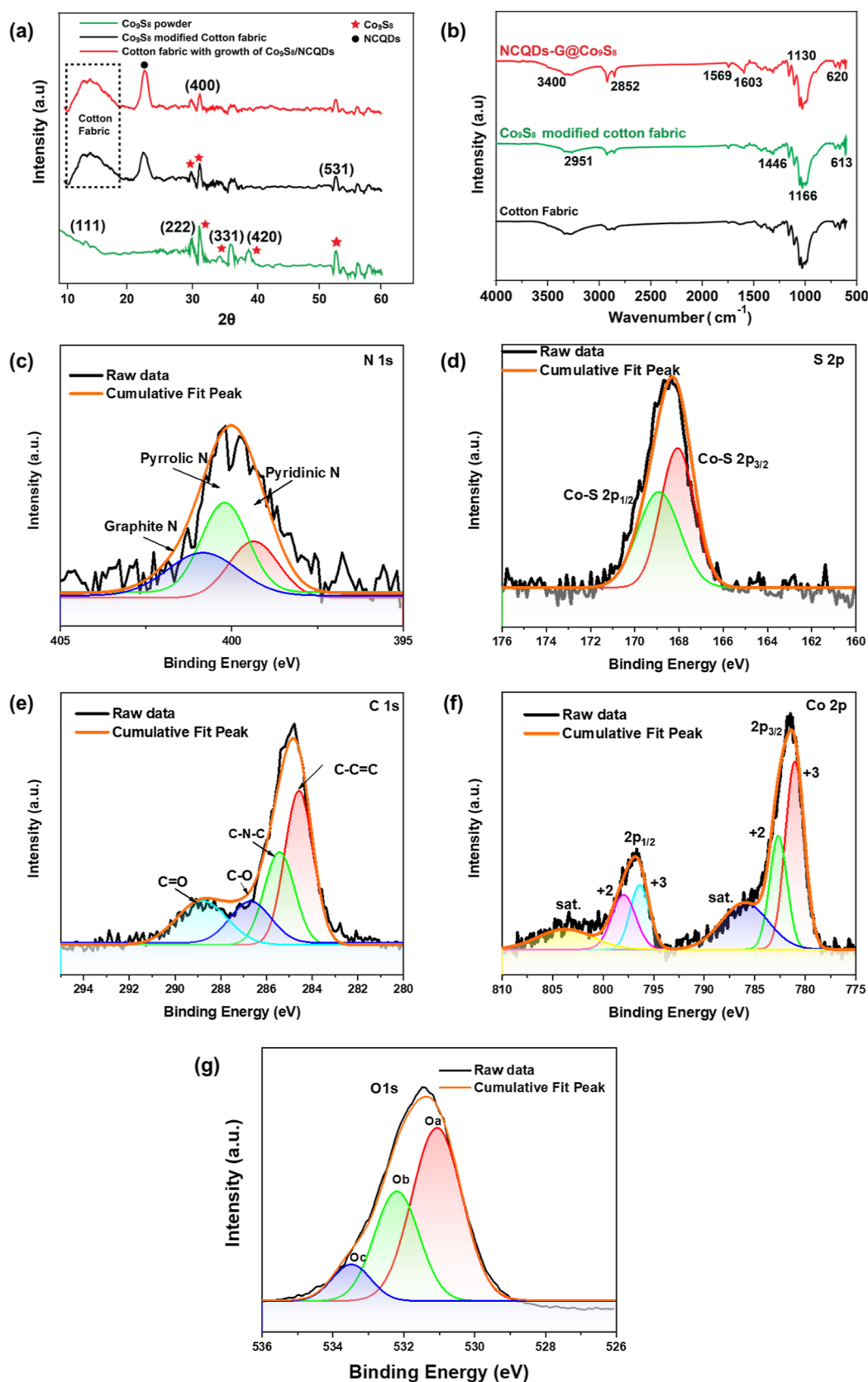
Figure 7. (a) XRD spectra of Co_9S_8 powder, Co_9S_8-modified fabric, and NCQDs-G@Co_9S_8. (b) FTIR spectra of cotton fabric, Co_9S_8-modified fabric, and NCQDs-G@Co_9S_8. (c−g) Deconvoluted XPS spectra of N, S, C, Co, and O of optimized NCQDs-G@Co_9S_8.

on the surface of active materials and hence hamper the interaction of active materials and pollutant molecules.[41]

SEM images of cobalt sulfide growth on fabric at a different resolution in Figure 5. Image (a) is a fabric image with the

growth of cobalt sulfide and image (b) is high-resolution image of image (a). Image (c,d) is the high-resolution image of the growth of cobalt sulfide on the fabric in nanosheet form. SEM images with the growth of Co_9S_8/NCQDs composite on cotton fabric have uniform growth of NCQDs and there is no change in the morphology of Co_9S_8 with the growth of NCQDs. As NCQDs size is very small, hence, it is difficult to detect via SEM; however, it was confirmed that there is no agglomeration of NCQDs. Therefore, to confirm the NCQDs on Co_9S_8, we used TEM analysis, as discussed in the next section.

The in situ growth of NCQDs on Co_9S_8 was observed using TEM. For that purpose, the fabric sample was set for severe sonication, which peeled off the composite from the fabric. TEM images show the spatial distribution growth of NCQDs on the fabric structure. Only NCQDs were also peeled off from the nanocomposite, as shown in Figure 6. These NCQDs exhibited a similar average diameter of 5−10 nm. The reactants concentration and time effect the size of CQDs, which was optimized in our case, yielding suitable NCQDs size. The contrast in the crystal fringes of the NCQDs and Co_9S_8 is visible in the high-resolution images which overlapped together and confirm the growth of NCQDs on Co_9S_8, forming an intimate interface. The interplanar spacing for all CQDs of TEM images was ∼0.20 nm confirmed using XRD. Surface structure and growth of NCQDs were confirmed by HTREM which shows the difference in fringes [Figure 6c]. Selected area electron diffraction (SAED) pattern is also added in the inset of HTREM which shows a bright ring with few sharp bright spots, indicating a mixture of amorphous and crystalline structure of the composite.[42] In Figure 8d, the circle shows the clear growth of NCQDs on cobalt sulfide. The average crystalline size of NCQDs was ∼6 nm, which is aligned with the size calculated from XRD. FFT image is added in the inset of Figure 6e.

XRD was employed to evaluate the crystal structure of the Co_9S_8 and associated composite structures. Figure 7a shows 15, 31, 36, 39, 40, and 55° peaks associated with Co_9S_8 powder, which are related to 111, 222, 400, 331, and 531 planes, as confirmed from JCPDs card no (65-1765). However, the Co_9S_8 formation exhibits two phases, one is Co_9S_8, and the secondary phase is Co_9S_8.[43] Compared to Co_9S_8 powder, the growth of Co_9S_8 on cotton fabric causes the formation of additional peak at 23°, which is associated with the crystal planes of the cotton fiber. The cotton fabric peak at 23° was confirmed from JCPDs card no (03-0226) and broad peak at 15° due to the polymeric crystal structure of cotton fabric. Formation of weak crystalline sulfides on cotton fabric is associated with the amine-mediated activation mechanism, that rapidly generates active sulfur species and promote fast nucleation and growth.[44] Also, after NCQDs growth on Co_9S_8, an additional peak was observed at 23°, related to the 202 crystal plane of NCQDs. The cotton fabric peak at 23° intensity slightly increased with the growth of NCQDs. The XRD pattern has shown Co_9S_8 peaks at 2θ of 15, 31, 36, 39, 40, and 55° are associated with 111, 222, 400, 331, and 531 planes. The NCQDs XRD pattern shows a significant peak centered at around 23°, which may be attributed to the crystal plane of 002. Crystalline size was measured using Scherrer equation, $L = K\lambda/\beta \cos \theta$. NCQD's crystal size is 6.2 nm and peak of NCQDs shows it has a partially crystalline structure.[45]

FT-IR confirmed the presence of functional groups in Co_9S_8/NCQDs composite. Figure 7b shows the cotton fabric peaks at 3400 and 3271 cm^{-1}, related to −OH and C−H bonds. The absence of a peak at 1728 cm^{-1}, property of the carboxyl group of hemicellulose. The symmetric bending CH_2 in cellulose is associated with the absorption band at 1428 cm^{-1}. In cellulose polysaccharides the bending vibrations of the C−H and C−O groups of aromatic rings are visible at 1359 and 1314 cm^{-1}, respectively. The bending vibrations of C−H and C−O, the intense peak vibrations detected at 1033 cm^{-1} are associated with the stretching vibrations of (CO) and (OH) in the polysaccharide of cellulose.[46] After the growth of Co_9S_8 on cotton fabric, the peak intensity decreases for the −OH peak, which is due to Co_9S_8 atoms replacing OH groups from the cotton fabric. These groups behave as a nucleation site for the growth of Co_9S_8. The peak at 613 cm^{-1} is associated with the Co_9S_8 bond, while the peak at 661 cm^{-1} is associated with polysulfide. Furthermore, the bending vibration of the sulfonated group is identified at 1603 and 1124 cm^{-1}, respectively. The stretching vibration of Co on the surface of Co_9S_8 is responsible for the peak at 620 cm^{-1}.[47] To authenticate the structure and composition of the NCQDs and Co_9S_8, the large absorption bands at 3400 and 3271 cm^{-1} in NCQDs-G@Co_9S_8 in (Figure 6b) are connected to the bending vibration of O−H and N−H, correspondingly.[48] The C−H bond stretching vibrations are shown by the prominent peak at 2852 cm^{-1}. The peaks at about 1558 and 1569 cm^{-1} are allocated to the usual stretching peaks of the C═N and N−H bonds, correspondingly. The absorption band at 1558 cm^{-1} exhibits the stretching vibrations peak of C═O.[38] These groups increase the adsorption process which enhances the PCA of the electrode by creating active sites.

X-ray photoelectron spectroscopy (XPS) was performed to elucidate the chemical bonding and composition. XPS spectrum confirmed the presence of C, N, S, O, and Co which shows that the atomic ratio of S/Co is around 1:1.09, consistent with the atomic ratio of S/Co in the chemical formula of Co_9S_8. Figure 7c,d shows various modes of nitrogen and sulfur. Detailed study of the bonding configuration of every component was additionally confirmed by high-resolution XPS spectra. The N 1s peak can be deconvoluted into three peaks, which represent pyridinic N (397.97 eV), pyrrolic N (399.9 eV), and graphitic N (402.1 eV). This reveals the presence of N doping within the graphitic carbon structure of NCQDs, formed on the surface of cobalt sulfide. Figure 7c shows the S 2p XPS spectrum for the NCQDs-G@Co_9S_8 in situ composites. In S 2p XPS spectrum, the raw curve associated with two different types of sulfur at 168.7 and 169.9 eV can be peak fitted into two curves which represent the Co−S 2p$^{3/2}$ and Co−S 2p$^{1/2}$, correspondingly. It is possible to deconvolute the high-resolution spectra of C 1s (Figure 7b) into numerous peaks that correspond to C═C−C (284.6 eV), C−N−C (285.3 eV), C−O (287.1 eV), and C═O (289.1 eV).[49,50] The peaks at 797.1 and 799.1 eV of Co 2p ascribed to the 2p$^{1/2}$ of Co^{+2} and Co^{3+}, respectively. The 2p$^{3/2}$ of Co^{2+} and Co^{3+} belong to peaks at 781.05 and 783.17 eV correspondingly, as well as the corresponding two shakeup satellites peaks (abbreviated as "Sat.").

The O 1s XPS spectra in Figure 7g show the non-stoichiometry of oxygen and related V*O vacancies or surplus O atoms. The O 1s region, in the energy range between 534 and 527 eV, was fitted with three peaks using a XPS fitting program. The three peaks observed in the O 1s binding energy region are located at 529.7 ± 0.4 eV (Oa), 530.6 ± 0.5 eV (Ob), and 531.8 ± 0.7 eV (Oc).
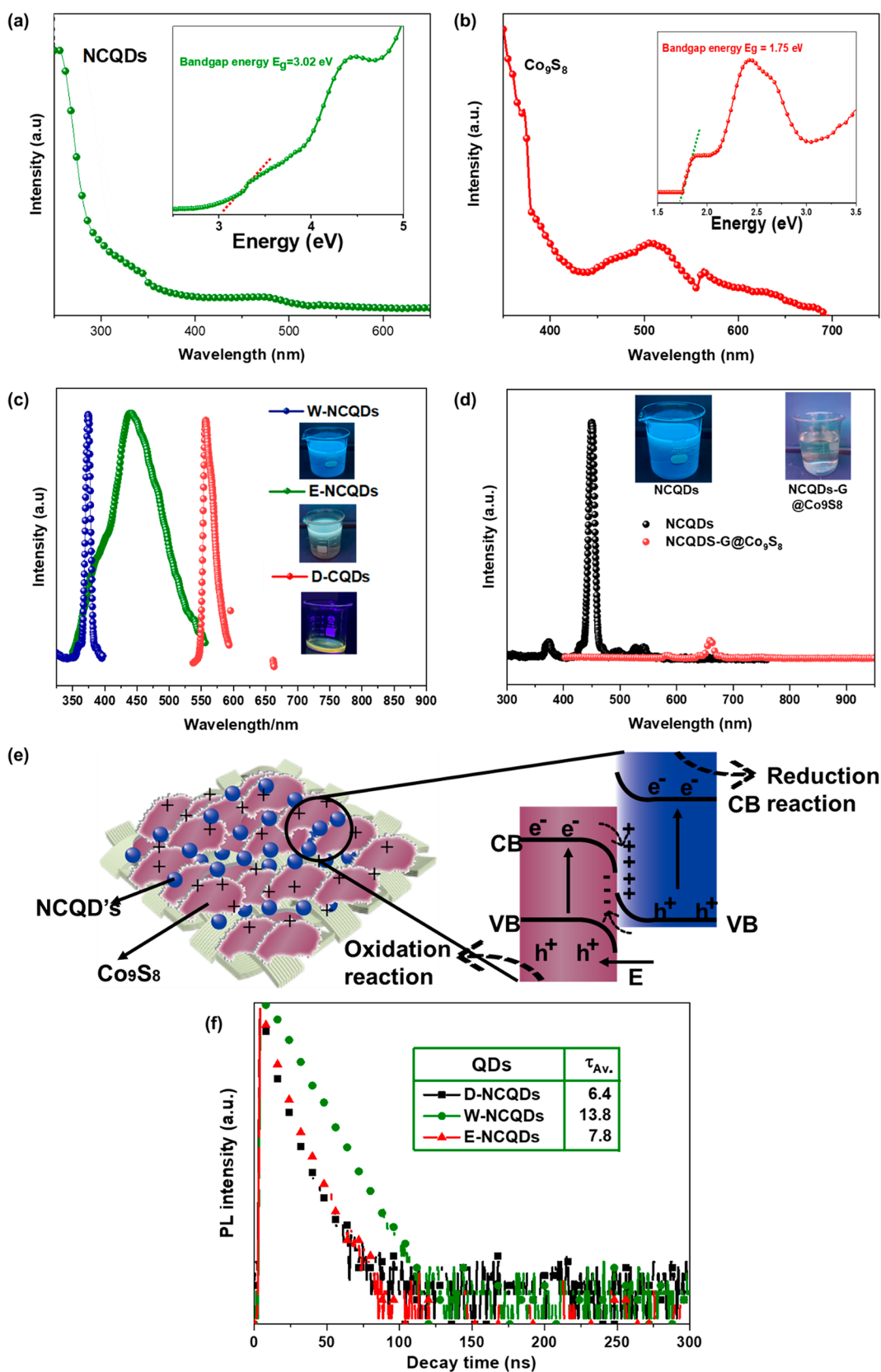
Figure 8. UV−visible absorption and Tauc plot of (a) NCQDs and (b) Co_9S_8 and (c) PL spectra of W-NCQDs, E-NCQDs, and D-NCQDs. (d) PL spectra of NCQDs and NCQDS-G@Co_9S_8 composite. (e) Degradation mechanism.

4.1. Mechanism of Nanocomposite Catalysis.

4.1.1. Optical Properties. An analysis of the optical properties of NCQDs-G@Co_9S_8 confirmed the presence of a surface-

state-dependent UV and visible light absorption. In Figure 8a, the UV−visible absorbance spectra of the NCQDs shows two sections related to $\pi-\pi^*$ transitions 250−360 nm range and

$n-\pi^*$ within 300–480 nm wavelength. It is worth noting that both $\pi-\pi^*$ and $n-\pi^*$ nitrogen doping results in visible light absorption of NCQDs. Undoped CQDs are only active in UV light; hence, lower photo absorption restricts their photo-activity to UV spectrum only. The HOMO−LUMO gap [inset of Figure 8a of NCQDs was calculated via Tauc plot, derived from UV−vis values using eq 4

$$\left[(\alpha h\nu)^{\frac{1}{n}} = C \times (h\nu - E_g) \right] \tag{4}$$

where $h\nu$ is the incident photon energy, C is the proportionality constant, E_g is the band gap energy, and $n = 1/2$ and 2 for direct and indirect band gap, correspondingly. Co_9S_8 is an indirect band gap material, and we suppose $n = 2$. The data within the absorption range of 249−550 nm was considered. From the linear part of the $(\alpha h\nu)^2$ versus $h\nu$ plot (inset, Figure 8b), for its band gap (1.7 eV). The curvature nearing the absorption edge could be due to defect sites or indirect transitions; therefore, visible light fluorescence was not detected for the Co_9S_8 sample.[51]

The fluorescence of CQDs is linked to their electronic band structure. The quantum confinement phenomenon and accompanying photoexcitation in NCQDs were confirmed by the PL spectra. Figure 8c depicts the emission of NCQDs, E-NCQDs, and D-NCQDs colloids under the excitation of 360 nm. The PL signal of W-NCQDs, E-NCQDs, and D-NCQDs were centered at 450, 475, and 550 nm wavelengths, respectively. The D-NCQDs have a higher content of surface states; therefore, the HOMO−LUMO gap was reduced. The HOMO−LUMO gap narrows as the surface states are increased by using organic solvents, resulting higher Stoke's shift.[52] According to their Stoke shift ranges, the W-NCQDs emitted blue light, while the E-NCQDs and D-NCQDs emitted yellowish-green light, as shown in photographic images of NCQDs colloid in Figure 8c.[53] Here, it is important to note that, although W-NCQDs have high energy emission and lower absorption range, however, their band alignment with Co_9S_8 is possible. This results in the formation of a heterojunctioned structure, where charges can efficiently be separated. PL spectra of NCQDs-G@Co_9S_8 show negligible emission as compared to NCQDs colloid Figure 8d, which confirmed the development of a heterojunction between NCQDs and Co_9S_8, reducing the recombination of electron hole pairs and enhancing the photocatalysis. Enhanced photocatalytic activity of the composite structure could be attributed to its better light absorption and extended lifetime. As from UV−vis analysis it is confirmed that the light absorption spectra of the nanocomposite is not enhanced. However, the enhanced activity of the composite could be related to its enhanced charge separation.[54]

To gain deeper insights into the role of surface states, we conducted charge recombination dynamics analysis using time-resolved photoluminescence (TRPL) measurements. The obtained decay time values were found to be triexponential, indicating that there is combination of radiative and non-radiative recombination's, responsible for the emissions [Figure 8f]. Interestingly, the average decay times ($\tau_{Av.}$) for W-NCQDs, E-NCQDs, and D-NCQDs were found to be 13.8, 7.8, and 6.4 ns, respectively. These differences in decay times suggest that the variation in surface states can be attributed to changes in the solvents used during the synthesis. Longer dwell time of W-CQDs showed better photocatalytic performance in the composite, showing that charge dwell time is more

important than light absorption, as E-NCQDs and D-CQDs has higher light absorption.

Thin layer chromatography (TLC) was performed using the optimal sample and MB dye to confirm the dye mineralization. Twenty mL solution of MB dye was prepared and the optimal sample was added in it. Degraded solution as shown in Figure S1b. To check the formation of intermediates, two TLC plates were prepared by casting the drops of simple MB dye and partially degraded dye solution. These TLC plates were placed in the 90:20% of chloroform and methanol solution for the formation of bands. The developed TLC plates images are added in Figure S1a which show that simple MB dye TLC plate shows one band and partially degraded dye TLC plate shows two bands which confirmed the presence of intermediates.

The optimal nanocomposite was tested for MB dye degradation in the presence of interfering/scavengers, including ethanol, ethylene diamine (EDA), sodium hydroxide, sodium carbonate, and sodium chloride species and placed the reaction mixture in visible light to check dye mineralization. EDA increased the catalytic activity of the electrode and dye was completely degraded. Sodium carbonate quench the OH groups present in composite which stop the degradation as shown in graph. The results confirm that OH groups participated in the degradation of the dye. Carbonate and bicarbonate ions are known $HO^\bullet$ scavengers. According to equations, they react with $HO^\bullet$ yielding $CO_3^{\bullet-}$, which is a less reactive radical. When NCQDs-G@Co9S8 is irradiated by sunlight, the possible radical species ($^\bullet OH$ and $O_2^\bullet$) can be generated. These radical species could degrade the MB dye to form several intermediate products that finally decompose into several nontoxic side products such as NH_2, CH_4, NO_2, SO_3, CO_2, and H_2O. Based on the reported study, the degradation of MB dye is through the decomposition of the chromophoric structure and the destruction of the homo and heteropoly aromatic rings that are presented in the MB structure. The electrons in the NCQDs-G@Co9S8 can be excited as the NCQDs-G@Co9S8 particles have narrow band gaps and contribute to the generation of free radical molecules. This leads to the discoloration and opening-ring reactions. The improvement of electron−hole transport channels has been constructed by the appropriate energy conduction or valence bands. Therefore, the highly feasible migration and separation of electrons and holes could be achieved during the photocatalytic degradation of MB dye.

$$Co_3^{2-} + HO^\bullet \rightarrow Co_3^{\bullet-} + HO^- \tag{5}$$

$$HCO_3^- + HO^\bullet \rightarrow Co_3^{\bullet-} + H_2O \tag{6}$$

These scavengers were added to the reaction and placed it into visible light to confirm the formation of intermediates during dye degradation. EDA increased the catalytic activity of electrode and dye was completely degraded. The other scavengers have similar results that means these reactive species are more contributing to photocatalysis except EDA, as shown in Figure S1d. When sodium carbonate was used as a scavenger minimum dye degradation occurred which shows that OH− species are the most active component in dye degradation.

The photocatalytic degradation mechanism of methylene blue (MB) dye solution catalyzed by NCQDs is illustrated in Figure. When the NCQDs-G@Co_9S_8 composite electrode is irradiated by sunlight, the possible radical species ($^\bullet OH$ and

$O_2^{\bullet}$) can be generated. These radical species could degrade the MB dye to form several intermediate products that finally decompose into several less toxic side products such as NH_2, CH_4, NO_2, SO_3, CO_2, and H_2O. The degradation of MB dye is through the decomposition of the chromophoric structure and the destruction of the homo- and heteropoly aromatic rings that are presented in the MB structure [Figure S2c]. The electrons in the NCQDs-G@Co$_9$S$_8$ can be excited and contribute to the generation of free radical molecules. This leads to the discoloration and opening- reactions. The improvement of electron–hole transport channels has been constructed by the appropriate energy conduction or valence bands. Therefore, the highly feasible migration and separation of electrons and holes could be achieved during the photocatalytic degradation of MB dye.

5. CONCLUSIONS

Most suitable coupling mode for the composite fabrication of Co$_9$S$_8$ and NCQDs was via direct heterogeneous stepwise growth. In addition, the heterogeneous growth on fabric suppresses the secondary contamination caused by the active material itself. The results reveal that the heterojunction structure formation and associated suitable charge separation is responsible for improved photocatalytic activity of the electrode. The surface states of NCQDs formed using water solvent were most compatible despite having a higher band gap. The highest dye degradation of 92% was observed for 0.20 wt % of NCQDs. This performance was further enhanced to 97% under slightly basic conditions, showing the major contribution from −OH groups in photocatalysis. In addition, the electrode showed significant Cr(IV) reduction, confirming its suitability for inorganic pollutants as well. The proposed direct growth of NCQDs omits the requirement for the complex purification of NCQDs, such as dialysis membrane and silica gel chromatography. Based on facile processing, we expect our proposed strategy will advance the scalable synthesis of active photocatalysts.

ASSOCIATED CONTENT

Ⓢ Supporting Information

The Supporting Information is available free of charge at https://pubs.acs.org/doi/10.1021/acsomega.3c03407.

Effect of solution pH on the degradation kinetics graph, comparison of dye degradation using different photocatalysts, and structure of NCQDs (PDF)

AUTHOR INFORMATION

Corresponding Author

Muhammad Imran Yousaf − *Department of Applied Sciences, National Textile University, Faisalabad 37610, Pakistan;* ⓞ orcid.org/0000-0003-3458-7113; Email: imran@ntu.edu.pk

Authors

Kinza Shahid − *Department of Applied Sciences, National Textile University, Faisalabad 37610, Pakistan*

Mubark Alshareef − *Department of Chemistry, Faculty of Applied Science, Umm Al Qura University, Makkah 24230, Saudi Arabia*

Mumtaz Ali − *Department of Textile Engineering, National Textile University, Faisalabad 37610, Pakistan*

Marwah M. Alsowayigh − *Chemistry Department, College of Science, King Faisal University, Al-Ahsa 31982, Kingdom of Saudia Arabia*

Imtiaz Afzal Khan − *Interdisciplinary Research Center for Membranes and Water Security, King Fahad University of Petroleum and Minerals (KFUPM), Dhahran 31261, Saudi Arabia*

Complete contact information is available at:
https://pubs.acs.org/10.1021/acsomega.3c03407

Notes

The authors declare no competing financial interest.

REFERENCES

(1) Ayodhya, D.; Veerabhadram, G. A review on recent advances in photodegradation of dyes using doped and heterojunction based semiconductor metal sulfide nanostructures for environmental protection,. *Mater. Today Energy* **2018**, *9*, 83−113.

(2) Police, A. K. R.; Vattikuti, S. P.; Mandari, K. K.; Chennaiahgari, M.; Phanikrishna Sharma, M. V.; Valluri, D. K.; Byon, C. Bismuth oxide cocatalyst and copper oxide sensitizer in Cu2O/TiO2/Bi2O3 ternary photocatalyst for efficient hydrogen production under solar light irradiation,. *Ceram. Int.* **2018**, *44* (10), 11783−11791.

(3) Ong, C. B.; Ng, L. Y.; Mohammad, A. W. A review of ZnO nanoparticles as solar photocatalysts: Synthesis, mechanisms and applications,. *Renew. Sustain. Energy Rev.* **2018**, *81*, 536−551.

(4) Bavar, S. M. R.; Alamolhoda, S.; Bafghi, M. S.; Masoudpanah, S. M. Photocatalytic performances of cobalt sulfides prepared by solution combustion synthesis using mixed fuels,. *J. Phys. Chem. Solids* **2021**, *149*, 109805.

(5) Yu, H.; Zhang, H.; Huang, H.; Liu, Y.; Li, H.; Ming, H.; Kang, Z. ZnO/carbon quantum dots nanocomposites: One-step fabrication and superior photocatalytic ability for toxic gas degradation under visible light at room temperature,. *New J. Chem.* **2012**, *36* (4), 1031−1035.

(6) Kristl, J.; Dojer, B. Synthesis of nickel and cobalt sulfide nanoparticles using a low cost sonochemical method. *Heliyon* **2017**, *3*, No. e00273.

(7) Samadi, M.; Zirak, M.; Naseri, A.; Kheirabadi, M.; Ebrahimi, M.; Moshfegh, A. Z. Design and tailoring of one-dimensional ZnO nanomaterials for photocatalytic degradation of organic dyes: a review. *Res. Chem. Intermed.* **2019**, *45*, 2197−2254.

(8) Zhou, Y.; Zahran, E. M.; Quiroga, B. A.; Perez, J.; Mintz, K. J.; Peng, Z.; Liyanage, P. Y.; Pandey, R. R.; Chusuei, C. C.; Leblanc, R. M. Size-dependent photocatalytic activity of carbon dots with surface-state determined photoluminescence. *Appl. Catal., B* **2019**, *248*, 157−166.

(9) Zhang, S.; Gao, M.; Zhai, Y.; Wen, J.; Yu, J.; He, T.; Kang, Z.; Lu, S. Which kind of nitrogen chemical states doped carbon dots loaded by g-C3N4 is the best for photocatalytic hydrogen production. *J. Colloid Interface Sci.* **2022**, *622*, 662−674.

(10) Zhao, C.; Wang, X.; Yu, L.; Wu, L.; Hao, X.; Liu, Q.; Lin, L.; Huang, Z.; Ruan, Z.; Weng, S.; et al. Quaternized carbon quantum dots with broad-spectrum antibacterial activity for the treatment of wounds infected with mixed bacteria. *Acta Biomater.* **2022**, *138*, 528−544.

(11) Qu, Z.; Wang, J.; Tang, J.; Shu, X.; Liu, X.; Zhang, Z.; Wang, J. Carbon quantum dots/KNbO 3 hybrid composites with enhanced visible-light driven photocatalytic activity toward dye waste-water degradation and hydrogen production. *Mol. Catal.* **2018**, *445*, 1−11.

(12) Jamila, G. S.; Sajjad, S.; Leghari, S. A. K.; Mehboob, M.; Flox, C. Enhanced electron transport by Fe2O3 on NCQDs-MgO nanostructure for solar photocatalysis and electrocatalytic water splitting. *Appl. Nanosci.* **2022**, *12* (6), 1815–1827.

(13) Alarifi, I. M.; Alharbi, A.; Khan, W. S.; Swindle, A.; Asmatulu, R. Thermal, electrical and surface hydrophobic properties of electrospun polyacrylonitrile nanofibers for structural health monitoring. *Materials* **2015**, *8* (10), 7017–7031.

(14) Batool, R.; Rhouati, A.; Nawaz, M. H.; Hayat, A.; Marty, J. L. A review of the construction of nano-hybrids for electrochemical biosensing of glucose. *Biosensors* **2019**, *9* (1), 46.

(15) Choi, K.; Seo, S.; Kwon, H.; Kim, D.; Park, Y. T. Fire protection behavior of layer-by-layer assembled starch-clay multilayers on cotton fabric. *J. Mater. Sci.* **2018**, *53* (16), 11433–11443.

(16) Zhou, J.; Lin, J.; Huang, X.; Zhou, Y.; Chen, Y.; Xia, J.; Wang, H.; Xie, Y.; Yu, H.; Lei, J.; et al. A library of atomically thin metal chalcogenides. *Nature* **2018**, *556* (7701), 355–359.

(17) Liang, Q.; Ma, W.; Shi, Y.; Li, Z.; Yang, X. Easy synthesis of highly fluorescent carbon quantum dots from gelatin and their luminescent properties and applications. *Carbon* **2013**, *60*, 421–428.

(18) Devi, S.; Kaur, A.; Sarkar, S.; Vohra, S.; Tyagi, S. Synthesis and characterization of highly luminescent N-doped carbon quantum dots for metal ion sensing. *Integr. Ferroelectr.* **2018**, *186* (1), 32–39.

(19) Zhou, J.; Liu, Y.; Zhang, S.; Zhou, T.; Guo, Z. Metal chalcogenides for potassium storage. *InfoMat* **2020**, *2* (3), 437–465.

(20) Zhang, Y.; Zhou, Q.; Zhu, J.; Yan, Q.; Dou, S. X.; Sun, W. Nanostructured Metal Chalcogenides for Energy Storage and Electrocatalysis. *Adv. Funct. Mater.* **2017**, *27* (35), 1–34.

(21) Vieira, K. O.; Bettini, J.; De Oliveira, L. F. C.; Ferrari, J. L.; Schiavon, M. A. Synthesis of multicolor photoluminescent carbon quantum dots functionalized with hydrocarbons of different chain lengths. *N. Carbon Mater.* **2017**, *32* (4), 327–337.

(22) Mahat, N. A.; Shamsudin, S. A.; Jullok, N.; Ma'Radzi, A. H. Carbon quantum dots embedded polysulfone membranes for antibacterial performance in the process of forward osmosis. *Desalination* **2020**, *493*, 114618.

(23) Singh, R.; Singh, R. K. Detection of Malachite Green in Water Using Edge Excited Label Free Fluorescent Probe NCQDs. *J. Fluoresc.* **2020**, *30* (6), 1281–1285.

(24) Wang, X.; Li, Y.; Li, T.; Jin, Z. Synergistic Effect of Bimetallic Sulfide Enhances the Performance of CdS Photocatalytic Hydrogen Evolution. *Adv. Sustainable Syst.* **2023**, *7* (1), 1–10.

(25) Vedhantham, K.; Girigoswami, A.; Harini, A.; Girigoswami, K. Waste water remediation using nanotechnology-a review. *Biointerface Res. Appl. Chem.* **2022**, *12* (4), 4476–4495.

(26) Li, Y.; Zhang, B. P.; Zhao, J. X.; Ge, Z. H.; Zhao, X. K.; Zou, L. ZnO/carbon quantum dots heterostructure with enhanced photocatalytic properties. *Appl. Surf. Sci.* **2013**, *279*, 367–373.

(27) Ali, M.; Anjum, A. S.; Riaz, R.; Bibi, A.; Sun, K. C.; Jeong, S. H. Unraveling the surface states related Stokes shift dependent electrocatalytic activity of N-doped carbon quantum dots for photovoltaic applications. *Carbon* **2021**, *181*, 155–168.

(28) Shen, R.; Zhang, L.; Chen, X.; Jaroniec, M.; Li, N.; Li, X. Integrating 2D/2D CdS/α-Fe2O3 ultrathin bilayer Z-scheme heterojunction with metallic β-NiS nanosheet-based ohmic-junction for efficient photocatalytic H2 evolution. *Appl. Catal., B* **2020**, *266*, 118619.

(29) Ali, M.; Riaz, R.; Anjum, A. S.; Sun, K. C.; Li, H.; Ahn, S.; Jeong, S. H.; Ko, M. J. Microwave-assisted ultrafast in-situ growth of N-doped carbon quantum dots on multiwalled carbon nanotubes as an efficient electrocatalyst for photovoltaics. *J. Colloid Interface Sci.* **2021**, *586*, 349–361.

(30) Al Qamshouai, R. H.; Ahmed, A. M. A.; Alsaid, A. A. I.; Akhtar, M. S.; Al-Touby, S. S. J.; Hossain, M. A. Assessment of toxic normal saturated hydrocarbons in the Arabian seawater and Omani freshwater samples using liquid chromatography-mass spectrometry. *J. Umm Al-Qura Univ. Appl. Sci.* **2023**, *9* (1), 87–95.

(31) Wang, R. C.; Lu, J. T.; Lin, Y. C. High-performance nitrogen doped carbon quantum dots: Facile green synthesis from waste paper

and broadband photodetection by coupling with ZnO nanorods. *J. Alloys Compd.* **2020**, *813*, 152201.

(32) Wei, L.; Yu, C.; Yang, K.; Fan, Q.; Ji, H. Recent advances in VOCs and CO removal via photothermal synergistic catalysis. *Chin. J. Catal.* **2021**, *42* (7), 1078–1095.

(33) Mogharbel, R. T.; Alkhamis, K.; Felaly, R.; El-Desouky, M.; El-Bindary, A.; El-Metwaly, N. M.; El-Bindary, M. Superior adsorption and removal of industrial dye from aqueous solution via magnetic silver metal-organic framework nanocomposite. *Environ. Technol.* **2023**, 1–17.

(34) Wang, Z.; Cheng, B.; Zhang, L.; Yu, J.; Li, Y.; Wageh, S.; Al-Ghamdi, A. A. S-Scheme 2D/2D Bi2MoO6/BiOI van der Waals heterojunction for CO2 photoreduction. *Chin. J. Catal.* **2022**, *43* (7), 1657–1666.

(35) Shen, R.; Zhang, L.; Li, N.; Lou, Z.; Ma, T.; Zhang, P.; Li, Y.; Li, X. W-N bonds precisely boost Z-scheme interfacial charge transfer in g-C3N4/WO3 heterojunctions for enhanced photocatalytic H2 evolution,. *ACS Catal.* **2022**, *12* (16), 9994–10003.

(36) Jiang, G.; Jiang, T.; Li, X.; Wei, Z.; Du, X.; Wang, X. Boronic acid functionalized N-doped carbon quantum dots as fluorescent probe for selective and sensitive glucose determination,. *Mater. Res. Express* **2014**, *1* (2), 025708.

(37) Liu, Y.; Li, W.; Wu, P.; Ma, C.; Wu, X.; Xu, M.; Luo, S.; Xu, Z.; Liu, S. Hydrothermal synthesis of nitrogen and boron co-doped carbon quantum dots for application in acetone and dopamine sensors and multicolor cellular imaging,. *Sens. Actuators, B* **2019**, *281*, 34–43.

(38) Liu, W.; Jia, H.; Zhang, J.; Tang, J.; Wang, J.; Fang, D. Preparation of nitrogen-doped carbon quantum dots (NCQDs) and application for non-enzymatic detection of glucose,. *Microchem. J.* **2020**, *158*, 105187.

(39) Mei, Z.; Wang, G.; Yan, S.; Wang, J. Rapid microwave-assisted synthesis of 2D/1D ZnIn2S4/TiO2 S-scheme heterojunction for catalyzing photocatalytic hydrogen evolution. *Acta Phys.-Chim. Sin.* **2020**, *37* (6), 2009097.

(40) Gao, R.; et al. Pyrene-benzothiadiazole-based polymer/CdS 2D/2D organic/inorganic hybrid S-scheme heterojunction for efficient photocatalytic H2 evolution. *Chin. J. Struct. Chem.* **2022**, *41* (6), 2206031–2206038.

(41) Bai, J.; Shen, R.; Jiang, Z.; Zhang, P.; Li, Y.; Li, X. Integration of 2D layered CdS/WO3 S-scheme heterojunctions and metallic Ti3C2MXene-based Ohmic junctions for effective photocatalytic H2 generation,. *Chin. J. Catal.* **2022**, *43* (2), 359–369.

(42) Arshad, Z.; Ali, M.; Lee, E. J.; Alshareef, M.; Alsowayigh, M. M.; Shahid, K.; Shahid, R.; Lee, K. H. Comparison of Electrospun Titania and Zinc Oxide Nanofibers for Perovskite Solar Cells and Photocatalytic Degradation of Methyl Orange Dye,. *Catalysts* **2023**, *13* (7), 1062.

(43) Zhang, H.; Li, Y.; Zhang, G.; Xu, T.; Wan, P.; Sun, X. A metallic CoS2 nanopyramid array grown on 3D carbon fiber paper as an excellent electrocatalyst for hydrogen evolution,. *J. Mater. Chem. A* **2015**, *3* (12), 6306–6310.

(44) Salavati-Niasari, M.; Sabet, M.; Esmaeili, E. Synthesis and characterization of CoS2 nanostructures via hydrothermal method,. *Synth. React. Inorg., Met.-Org., Nano-Met. Chem.* **2015**, *45* (8), 1159–1167.

(45) Ju, S.; Liu, Y.; Chen, H.; Tan, F.; Yuan, A.; Li, X.; Zhu, G. In situ Surface Chemistry Engineering of Cobalt-Sulfide Nanosheets for Improved Oxygen Evolution Activity,. *ACS Appl. Energy Mater.* **2019**, *2* (6), 4439–4449.

(46) Alsulami, Q. A.; Arshad, Z.; Ali, M.; Wageh, S. Efficient Tuning of the Opto-Electronic Properties of Sol−Gel-Synthesized Al-Doped Titania Nanoparticles for Perovskite Solar Cells and Functional Textiles. *Gels* **2023**, *9*, 101.

(47) Wan, H.; Ji, X.; Jiang, J.; Yu, J.; Miao, L.; Zhang, L.; Bie, S.; Chen, H.; Ruan, Y. Hydrothermal synthesis of cobalt sulfide nanotubes: The size control and its application in supercapacitors,. *J. Power Sources* **2013**, *243*, 396–402.

(48) Arshad, Z.; Wageh, S.; Maiyalagan, T.; Ali, M.; Arshad, U.; Noor-ul-ain; Qadir, M. B.; Mateen, F.; Al-Sehemi, A. G. Enhanced charge transport characteristics in zinc oxide nanofibers via Mg2+ doping for electron transport layer in perovskite solar cells and antibacterial textiles,. *Ceram. Int.* **2022**, *48*, 24363−24371.

(49) Liu, S.; Wang, Z.; Zhou, S.; Yu, F.; Yu, M.; Chiang, C.; Zhou, W.; Zhao, J.; Qiu, J. Metal-Organic-Framework-Derived Hybrid Carbon Nanocages as a Bifunctional Electrocatalyst for Oxygen Reduction and Evolution,. *Adv. Mater.* **2017**, *29* (31), 1−10.

(50) Cao, Z.; Wu, M.; Hu, H.; Liang, G.-j.; Zhi, C.-y. Monodisperse Co 9 S 8 nanoparticles in situ embedded within N, S-codoped honeycomb-structured porous carbon for bifunctional oxygen electro-catalyst in a rechargeable Zn - air battery,. *NPG Asia Mater.* **2018**, *10*, 670−684.

(51) Chakraborty, I.; Malik, P. K.; Moulik, S. P. Preparation and characterisation of CoS2 nanomaterial in aqueous cationic surfactant medium of cetyltrimethylammonium bromide (CTAB),. *J. Nano-particle Res.* **2006**, *8* (6), 889−897.

(52) Tan, J.; Zou, R.; Zhang, J.; Li, W.; Zhang, L.; Yue, D. Large-scale synthesis of N-doped carbon quantum dots and their phosphorescence properties in a polyurethane matrix,. *Nanoscale* **2016**, *8* (8), 4742−4747.

(53) Miao, X.; Yue, X.; Ji, Z.; Shen, X.; Zhou, H.; Liu, M.; Xu, K.; Zhu, J.; Zhu, G.; Kong, L.; et al. Nitrogen-doped carbon dots decorated on g-C3N4/Ag3PO4 photocatalyst with improved visible light photocatalytic activity and mechanism insight,. *Appl. Catal., B* **2018**, *227*, 459−469.

(54) Guo, X.; Chang, C.; Wang, G.; Hao, X.; Jin, Z. CoV-LDH-Derived CoP$_2$ Active Sites and Zn$_x$Cd$_{1−x}$S Solid-Solution Ingeniously Constructed S-Scheme Heterojunction for Photocatalytic Hydrogen Evolution. *Adv. Sustainable Syst.* **2023**, *7* (1), 1−14.